223 (2023) 211569

Contents lists available at ScienceDirect

Geoenergy Science and Engineering

journal homepage: www.sciencedirect.com/journal/geoenergy-science-and-engineering

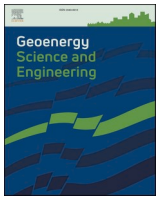

The impact of permeability barriers on steam-solvent coinjection – A mechanistic study using a physical model

Kai Sheng [a], Ryosuke Okuno [a,*], Abdullah Al-Gawfi [b], Petro Nakutnyy [b]

[a] The University of Texas at Austin, USA
[b] Saskatchewan Research Council, Canada

ARTICLE INFO

Keywords:
Steam-assisted gravity drainage
Bitumen
Steam-solvent coinjection
Heterogeneity
Steam chamber

ABSTRACT

Coinjection of steam and condensate has been studied for improving the energy efficiency of steam-assisted gravity drainage (SAGD) as solvent-assisted SAGD or SA-SAGD. However, it is not well understood how tortuous hydraulic paths under heterogeneous permeability can influence the compositional and thermal flow characteristics in SA-SAGD. We addressed this question by performing an experiment of the coinjection of steam and condensate for bitumen recovery. This paper discusses the experimental results and gives our mechanistic analysis of how the tortuous hydraulic paths affected the thermal and compositional flow and the properties of the produced bitumen in the experiment.

The physical model was a cylindrical pressure vessel with a diameter of 0.425 m and a length of 1.2 m, which was filled with unconsolidated sands. Two shale plates were horizontally installed above the well pair at different elevations so that they could represent permeability barriers to cause tortuous flow paths during the SA-SAGD experiment. The porosity and permeability of the sandpack was 0.34 and 5.6 D, respectively. Initially, the oil and water saturations were 95% and 5%, respectively.

After preheating for 1 day, a mixture of 98.2 mol% steam and 2.8 mol% condensate was injected at 3500 kPa for 4 days (35 cm^3/min of steam, cold water equivalent). The injection and production histories along with the real-time temperature distribution were recorded during the experiment. Produced oil samples were frequently taken and analyzed for density and asphaltene content. After the experiment, the sandpack was excavated and sampled from different locations to analyze the saturation and asphaltene content of the remaining oil. The experimental results in this paper were compared with the previous SAGD and SA-SAGD experiments that used the same experimental set up with a homogeneous sandpack.

Results showed that, in comparison to the homogeneous SAGD case, SA-SAGD was able to lower the cumulative steam-oil ratio (SOR) by a factor of two to three even in the presence of shale plates. Analysis of the temperature profiles indicated that the steam chamber vertically expanded from the lower part to the upper part through tortuous paths at lower temperatures. An emerging steam chamber above the shale plates occurred by convective heat from the injection well through lower-temperature flow paths between shale plates, involving light to intermediate solvent components that enabled the steam chamber to expand away from the injection well. This highlights the important role of volatile solvent components in the growth of a steam chamber in SA-SAGD under heterogeneity. The produced bitumen density in this research was closer to the original bitumen than in the homogeneous SA-SAGD case because the bitumen dilution and the solvent retention increased by the tortuous flow regime resulted in efficient drainage of oil at lower temperature.

1. Introduction

Steam-assisted gravity drainage (SAGD) has been widely used for bitumen recovery, but it is an energy-intensive process requiring a large amount of high-quality steam. Improving the energy efficiency of SAGD has become important for environmental concerns. The cumulative steam-oil ratio (CSOR) is often used to evaluate the energy efficiency of SAGD, which is the volume ratio of the injected water to the produced oil. Among many other factors, CSOR smaller than 4 m^3/m^3 is considered economically feasible (Shen, 2013).

Solvent-assisted SAGD (SA-SAGD) injects steam with volatile

* Corresponding author. Department of Petroleum and Geosystems Engineering, 200 E. Dean Keeton Street, Stop C0300, Austin, TX, 78712, USA.
E-mail address: okuno@utexas.edu (R. Okuno).

https://doi.org/10.1016/j.geoen.2023.211569
Received 14 September 2022; Received in revised form 6 January 2023; Accepted 8 February 2023
Available online 10 February 2023

Nomenclature

Abbreviations

CMG	Computer Modeling Group
CWE =	cold water equivalent volume
PR EOS =	Peng-Robinson equation of state
SAGD =	steam-assisted gravity drainage
SA-SAGD =	solvent-assisted steam-assisted gravity drainage
SRC =	Saskatchewan Research Council

hydrocarbon solvent, aiming to increase the efficiency of SAGD. The injected solvent propagates as part of the vapor phase and condenses near the edge of a steam chamber. The bitumen mobility is increased by the dilution with condensed solvent. The volatile components may condense and vaporize across the chamber interface, while enhancing the oil drainage. This mechanism is often referred to as distillation in steam injection (Prats, 1982). The vaporization and condensation of solvent components have been considered an important mechanism in the SA-SAGD research (Dong, 2012; Hosseininejad Mohebati et al., 2012; Keshavarz et al., 2014, 2015; Venkatramani and Okuno, 2017, 2018a; Sheng et al., 2018; Ovalles, 2019; Zirahi et al., 2020). The choice of solvent for SA-SAGD has been studied for optimizing the SA-SAGD operations in terms of oil recovery and energy efficiency.

The possibility of using diluent, an economic alternative to intermediate alkane solvents (e.g., hexane), has been investigated in the literature (Al-Murayri et al., 2016a, 2016b; Ayodele et al., 2009; Jha et al., 2013; Khaledi et al., 2012, 2015). Such diluents are hydrocarbon mixtures, such as condensate and naphtha. Nasr et al. (2003) have shown that coinjection of steam and condensate resulted in similar oil production rates to hexane-SAGD. Al-Murayri et al. (2016a, 2016b) studied the use of naphtha and condensate in their SA-SAGD experiments and investigated the impact of multicomponent solvents on asphaltene precipitations. Ayodele et al. (2009) investigated the impact of operating pressure and condensate concentration on oil recovery and energy efficiency. They concluded that condensate at a low concentration could be effective at low operating pressures, with a significant reduction in heat loss to the overburden. Khaledi et al. (2012, 2015) conducted SA-SAGD experiments using two types of condensates. Their condensates showed very different carbon-number distributions, but the majority of the carbon number fell between 6 and 10. Their results did not indicate a significant difference in the performance of the two condensates.

Using multicomponent solvents makes the compositional flow in SA-SAGD more involved. The mechanisms of oil recovery by using multicomponent hydrocarbon solvents have been investigated through numerical simulation in the literature. Deng et al. (2010) investigated the compositional distribution of condensate components when the condensate was injected into a 2-D homogeneous reservoir model. Their results showed that the heavier condensate components propagated at a slower rate with the steam chamber. Sheng et al. (2021a) investigated the compositional details of steam-condensate coinjection into a 3-D heterogeneous reservoir and the role of each condensate species in the process. They characterized the condensate using methane and three pseudo components, S1 (C_4-like), S2 (C_8-like), and S3 (C_{21}-like). They confirmed that the solvent species propagated at a different rate in the reservoir according to the volatility. Their analysis indicated that S2 was the main solvent utilized for dilution, and methane and S1 improved the conformance of a steam chamber by accumulating in the steam chamber.

Besides the compositional complexity of condensates, reservoir heterogeneity is another major uncertainty for the economic feasibility of SA-SAGD. Many papers in the literature discussed the impact of the shale facies distribution on the energy and oil-recovery efficiency. Gotawala and Gates (2010) studied the impact of the dimensions of permeability barriers on the steam-chamber growth in SAGD through 3-D numerical simulations constructed with variograms. They concluded that for a typical Athabasca oil sand reservoir, the correlation length of permeability barriers of about 200 m would result in the maximum steam chamber growth. They suggested that well pairs should be positioned where the correlation range was close to this value. Ma and Leung (2020) studied the impact of permeability barriers on the SAGD production history, such as temperature and oil-recovery factor. They used data analytics and deep learning techniques to rapidly establish correlations between shale distribution and production history. Kumar and Hassanzadeh (2021a, 2021b) performed many 2-D SAGD simulations to examine the impact of the shale facies on oil recovery. They showed that there existed a threshold for the shale volume fraction that would negatively impact oil recovery. Huang et al. (2019) conducted a SAGD experiment in a heterogeneous sandpack with four equal-length and paralleled permeability barriers above the injectors. They performed history-matching of the results and sensitivity analysis of the shale length and the interval between shales. Their results indicated that a large SOR would occur when the chamber growth was adversely affected by permeability barriers at the early stage of SAGD.

The literature is much scarcer on the impacts of reservoir heterogeneity on the flow characteristics and performance of SA-SAGD. Venkatramani and Okuno (2018a, 2018b) studied the characteristics of in-situ flow and SOR of SAGD and hexane-SAGD using 2-D realizations generated for Athabasca bitumen reservoirs. Their simulation results showed that SAGD SOR ranged from 3 to 12 m^3/m^3, while SOR for hexane-SAGD ranged from 2 to 7 m^3/m^3 depending on the shale distribution. Sheng et al. (2021a) discussed the thermal/compositional effects of permeability barriers based on SA-SAGD simulations with stochastically generated 3-D reservoir realizations. Their simulation results showed that the permeability barriers reduced the separation of components by enhancing the mixing of oil and solvent and suppressing the impact of distillation. However, these conclusions were based solely on numerical reservoir simulations.

This paper reports an SA-SAGD experiment using condensate in a large heterogeneous physical model, where two horizontal shale plates caused the flow paths to be tortuous in the sandpack. This is the final part of the experiments of SAGD and SA-SAGD using the same experimental setup presented in Sheng et al. (2020, 2021b).

The first paper from this series of experiments (Sheng et al., 2020) presented the in-situ flow regimes and the impact of temperature on the produced oil properties. The high-temperature steam in SAGD vaporized the light fractions in the residual bitumen and resulted in a lighter produced bitumen than the original bitumen. At the initial stage of oil recovery, the oil-water counter-current flow was indicated by a large amount of oil production without expanding a steam chamber. Then, the numerical history matching of the experimental data identified the importance of including capillary pressure for modeling oil recovery in the early stage of SAGD.

The second paper from this series of experiments (Sheng et al., 2021b) was focused on the impact of the steam-solvent coinjection on the in-situ flow regime and the produced oil properties. Results showed that the solvent (condensate) enabled the steam chamber to expand more rapidly by establishing gravity-dominant flow. The dominant flow regime in the experiment was the co-current flow of water and oil, in contrast to the SAGD experiment.

The main objective of the current paper was to study the impact of permeability barriers on the in-situ thermal/compositional flow and the produced fluid properties in SA-SAGD using condensate. The experimental data were used to calibrate a numerical simulation model by matching the temperature profiles and the material balance of water,

bitumen, and condensate. The calibrated simulation model was used to understand the impact of permeability barriers in SA-SAGD.

In what follows, the experimental methods are described first. Then, the experimental results are discussed and analyzed by numerical simulation.

2. Methods for SA-SAGD experiment

This section first describes the experimental model and fluids used for the experiments. The procedures for the SA-SAGD experiment are then explained in detail, including preheating, wind down, fluid collection during the steam/solvent injection, and model degassing and excavation after the injection period. Since this is the last of the series of experiments using the same physical model, the experimental design largely followed Sheng et al. (2020, 2021b).

3. Experimental setup

Fig. 1 illustrates the SA-SAGD experimental setup [Saskatchewan Research Council (SRC)]. The model contained a pressure vessel, two flanges, a pair of horizontal wells, thermocouples, and inline heaters with thermocouples on the surface of heaters for the injection and production wells. Besides, the experiment system contained a steam generator, pumps capable of delivering water and solvent at a constant rate and high pressure, two production tanks, a gas chromatography for analyzing the produced gas, pressure gauges, and a gas meter to read the effluent gas volume. All operational parameters were recorded through a central data acquisition system.

The inner diameter and the length of the cylindrical vessel were 0.425 m and 1.22 m, respectively. Perforated stainless steel tubes were used as injection and production wells. The injector and producer were installed at 0.12 m and 0.04 m from the bottom of the cylindrical model, respectively (Fig. 2a). The well pair was wrapped with stainless-steel meshes to prevent sand production. The temperatures on 5 planes were measured by a total of 19 thermocouple strings (Fig. 2b). The heat loss during the experiment was controlled by band heaters and ceramic wool around the cylindrical vessel.

3.1. Fluid properties

The bitumen used was the same Athabasca bitumen as in Sheng et al., 2020, 2021b, of which the molar mass was 560 g/mol and the density was 1015 kg/m^3 at standard conditions. Appendix A gives more detailed properties of the bitumen sample.

The condensate sample had a molecular weight of 98 g/mol and a density of 703 kg/m^3. The carbon number distribution of the condensate ranged from C_3 to C_{60}. Appendix A gives the condensate properties, including carbon number distribution, viscosity, and density.

4. Experimental procedures

4.1. Sandpack model preparation

The heterogeneous sandpack was made by unconsolidated sands and two shale plates installed at locations shown in Fig. 2a. The sandpack consisted of 303 kg of unconsolidated sand of the same particle size distribution as in Sheng et al. (2020). This gave a porosity of 0.34 and a permeability of 5.6 D for the sand facies. The shale plates were made of Mancos shale with an averaged permeability of 8×10^{-5} mD (Kocurek Industries). The shale plates were 42.5 cm in length, which was the same as the sandpack, 0.794 cm (5/16 inches) in thickness, and 17.8 cm and 12.7 cm in width as shown in Fig. 2a. The distance between the flange and the shale plates on each side of the physical model was negligibly small.

The locations of the shale plates were determined through preliminary simulations to decelerate the steam chamber growth and to decrease the oil production rate while not making the experiment too complicated. The placement of the shale plates was to see the impact of tortuous flow paths on the flow characteristics, and to mechanistically understand the benefits of using solvents in such a situation.

Packing of sands was done after installing one of the flanges (the right end in Fig. 2). For the packing, the vessel was oriented vertically. The shale plates were placed exactly at the designed locations using a plastic guide. The plastic guide was a piece of thin plastic material that was specially designed for the shale plates used in this experiment. It had holes that tightly fit the dimensions of the shale plates, to prevent the shale plate from moving while pouring the sand and compacting it. Then, the sand was poured into the model in batches and compacted the sand using a submersible cement vibrator. Once the first batch was poured and compacted, the guide was lifted a few inches and the second patch of sand was poured and compacted. The process was repeated till the model was fully packed to the top. Then, the model was closed by the top flange as illustrated on the left side in Fig. 2.

The model was evacuated and checked for leakage after packing the sand. Then, deionized water was used to saturate the model. The measured volume was 58.7 L for the pore space and 171.2 L for the total

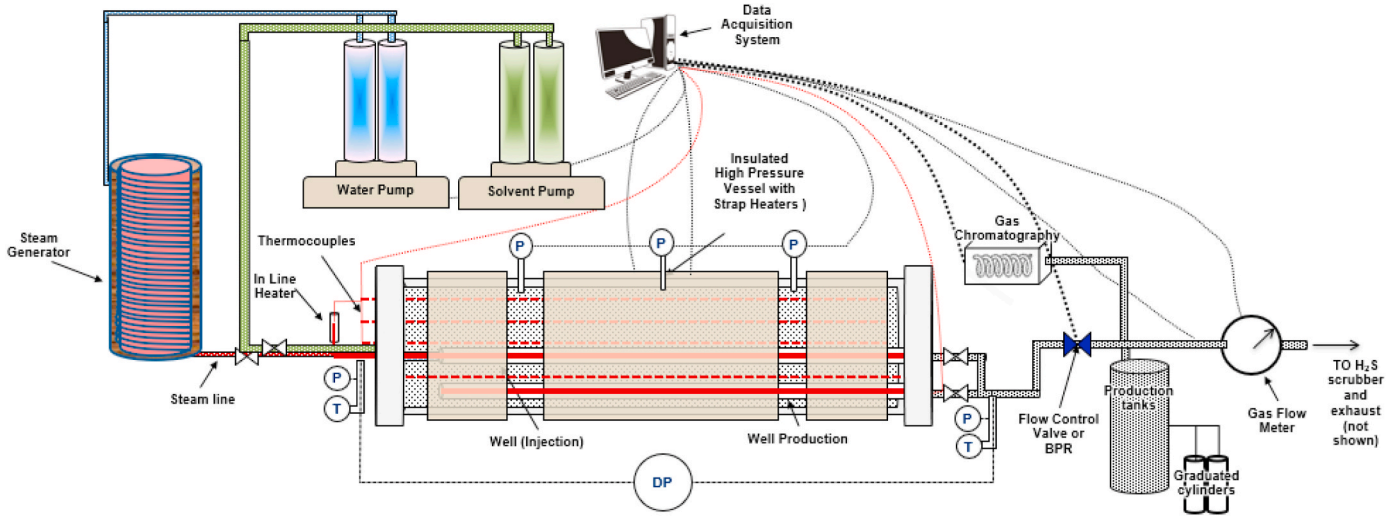

Fig. 1. Schematic of the setup for the SA-SAGD experiment. (BPR – Back pressure regulator, DP – Pressure transducer, P – Pressure gauges, T – thermometer, H_2S – hydrogen sulfide).

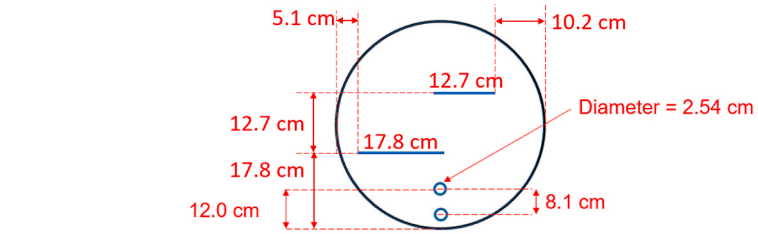

(a) A vertical cross-section of the physical model. The horizontal wells are shown by circles and the shale plates by blue bars.

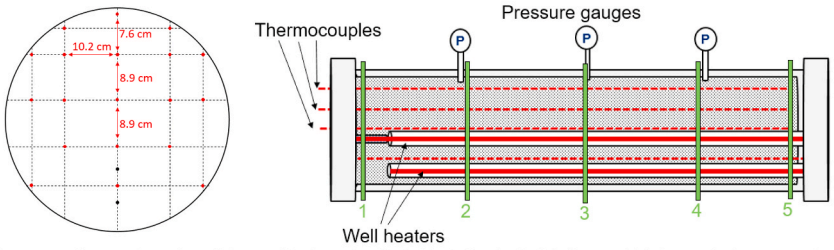

(b) Thermocouples are shown by red dots and horizontal wells by black dots in the left figure, which is a vertical cross-section of the model shown in the right figure.

Fig. 2. Specifications of the installed well pair and thermocouples for the SA-SAGD experiment. The injection (heel) side is on the left and the production (toe) side is on the right in the schematic of the cylindrical model.

space inside the pressure vessel. Then, the temperature of the model was increased to 75 °C. Thereafter, the bitumen heated to the same temperature was slowly injected from the bottom of the vessel. The total volume of injected bitumen was 55.5 L, which yielded an initial oil saturation of 94.6%.

4.2. Preheating the sandpack

The sandpack was preheated for 24 h. The inline heaters for the well pair gradually increased the temperature to and maintained at 125 °C. Meanwhile, the top and bottom band heaters were turned on to control the heat losses.

4.3. SA-SAGD experiment

After the preheating, steam injection was started with 35 cm^3/min [cold-water equivalent (CWE)] at 3500 kPa for 2.5 h to establish hydraulic communication between the wells. Then, steam and condensate were coinjected at a solvent concentration of 2.8 mol% (20 vol%). The corresponding water rate at 22 °C was 35 cm^3/min, and the solvent rate at 3500 kPa and 8 °C was 7.55 cm^3/min, respectively. The co-injection of steam and condensate continued for 96 h, during which the top and bottom band heaters were on for controlling heat losses.

The heat losses were controlled by approximating a no-energy-flow boundary condition via band heaters on the vessel surface. The band heater was programmed to control the temperature automatically to ensure the controlled energy input through the sandpack boundary. To avoid over-heating the sandpack, the heaters were controlled by an automated control logic based on the temperature readings immediately next to the model boundaries. This procedure minimized the energy flow across the boundary by approximating the band heater temperature to the temperature at the physical-model boundary.

To minimize the steam breakthrough in the experiment, temperatures in the producer were monitored. Band heaters at the bottom and the injector heaters were controlled to create a 5 to 10 °C subcool to maintain a liquid level near the producer, to avoid the steam breakthrough.

4.4. Ramp-down/cooling stage

The injection of steam and condensate was terminated after the SA-SAGD stage, and the upper and lower band heaters were made inactive. Pressurized nitrogen was delivered into the pressure vessel at 3500 kPa for 8 h, to remove the remaining solvent and hydrogen sulfide (H_2S) gas for the subsequent excavation of the sandpack. All produced fluids during the purging period were measured and analyzed. After the purging, the model pressure was reduced to atmospheric pressure.

4.5. Produced fluids collection

The production pressure of the system was maintained by a back-pressure regulator at approximately 3500 kPa as shown in Fig. 1. Two automated production tanks were used to alternatingly receive produced fluids that passed through the backpressure regulator, and to collect the oil and water production data. The accumulated steam and gases at the top of the tanks were condensed by forcing them through a condenser and a knock-out vessel. Dry gases were then separated and sent to a gas chromatography to analyze the composition. The produced dry gas volume was recorded through a wet test meter.

After a production tank was disconnected from the system, the produced liquids were drained from the bottom of the production tank to analyze the amount of water, bitumen and condensate. The cumulative volume and mass of water and oil production were recorded throughout the experiment.

4.6. Degassing and model excavation

The sandpack excavation was done after cooling down the physical model. The sandpack was divided into eight equal-length segments from the injection end to the production end and was excavated one by one. In each segment, five locations were sampled to analyze sands, water, oil, and asphaltenes contents.

5. Experimental Results and Discussion

Fig. 3 shows the cumulative weight of the produced liquid hydrocarbon. The bitumen recovery factor was 89.0% at 4320 min and 93.7%

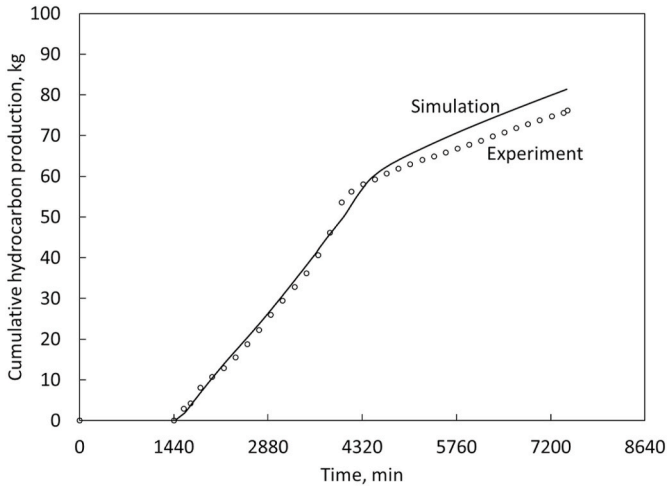

Fig. 3. Histories of cumulative hydrocarbon production in the oil phase at standard conditions from the SA-SAGD experiment and simulation.

around 5760 min. The solvent recovery factor was 73% at the end of the experiment. As shown in Appendix, however, there was an overlap in the carbon number distribution for condensate and bitumen; therefore, the amounts of the produced bitumen and condensate were estimated by first draining the automated production tanks into pails at specified intervals. The collected pails were cooled down to the ambient temperature. The free water was then poured off. Samples were taken from both the free water and the oil/condensate for analysis. After that, toluene was added to the remaining oil/condensate in the pails and heated to determine the remaining water in the oil. The collected oil/condensate samples were sent for analysis in terms of density, viscosity, and asphaltenes. The amount of condensate dissolved in oil was estimated using the density mixing rule with the measured densities for the original bitumen, condensate, and the mixtures of the two. Another stream of the gaseous condensate/steam was condensed in the knockout vessel and collected separately in graduated cylinders.

Fig. 4 shows that the injection and production of water were quite steady during the experiment. The difference between the injected and produced water at the end of the experiment was 9.2 L. The material balance of the water content was analyzed after the experiment. Approximately 4.9 L of water were retained in the sandpack, and 4.3 L

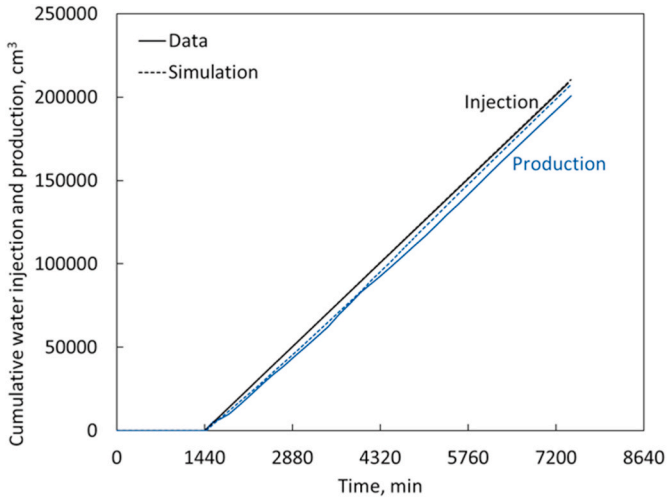

Fig. 4. Histories of cumulative water injection and production in the SA-SAGD experiment the history-matched numerical simulation. The dashed curves are the simulation results, and the solid curves are the experimental data. The injection and production curves are shown in black and blue, respectively.

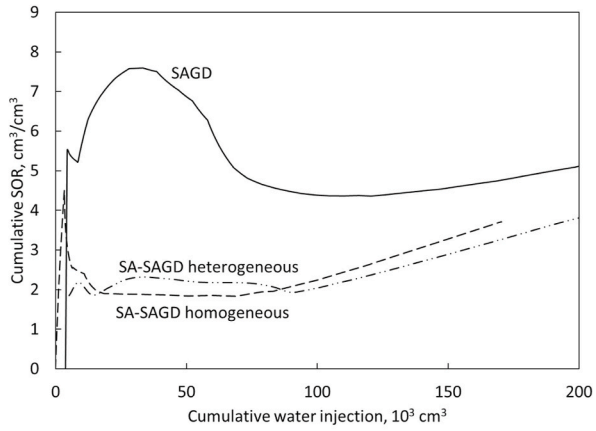

a. Histories of CSOR with respect to cumulative water injection

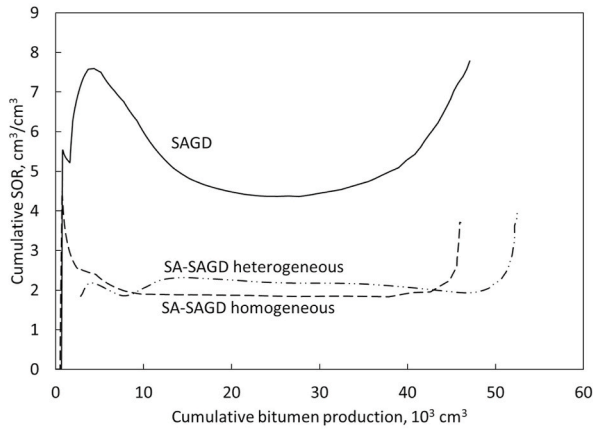

b. Histories of CSOR with respect to cumulative bitumen production

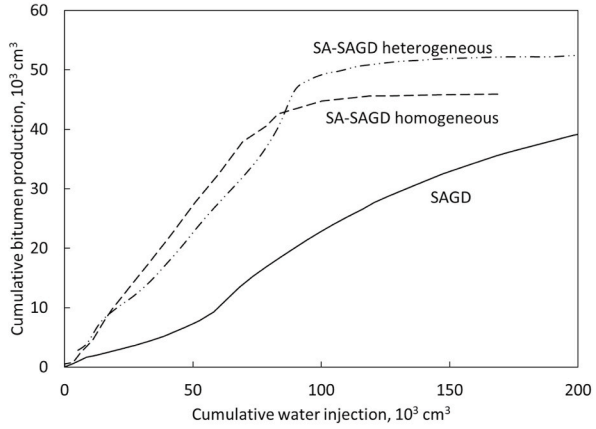

c. Histories of bitumen production with respect to cumulative water injection

Fig. 5. Equivalent CSOR for the SAGD and SA-SAGD in the homogeneous sandpacks (Sheng et al., 2020, 2021b) and SA-SAGD in the heterogeneous sandpack in this research.

(2% of the total injected water) could have been lost in the fluid handling. Fig. 5 presents the cumulative SOR for the current SA-SAGD experiment, in comparison to the previous homogeneous SA-SAGD and SAGD experiments [37–38]. Note that the water injection rate (35 cm^3/min) in the current experiment was smaller than the previous experiments (50 cm^3/min); therefore, the SORs are plotted against cumulative water injection (Fig. 5a), which represents the energy input through steam, and against the bitumen production (Fig. 5b), which correlates with the steam chamber size. The SOR in the current SA-SAGD experiment was smaller than the homogeneous SAGD by 2–3 cm^3/cm^3, but greater than the homogeneous SA-SAGD by 0.5 cm^3/cm^3. That is,

the impact of the permeability barriers on the flow regime was significant enough to increase the cumulative SOR by 25% from the homogeneous SA-SAGD. Fig. 5c compares the cumulative bitumen production with respect to cumulative water injection. The ultimate oil recovery in the heterogeneous sandpack was approximately 16% greater than in the homogeneous sandpack. This is likely because a real condensate (diluent) was used in the current paper, while the condensate used in the homogeneous experiment was a synthetic condensate using n-alkanes. The oil production rate of the SA-SAGD in the heterogeneous sandpack was approximately 20% smaller than that in the homogeneous sandpack. As will be shown later in this paper, the shale barriers effectively created tortuous oil flow, slowed down the oil production, and thus resulted in a higher SOR in comparison to the homogeneous case.

Fig. 6 shows temperature contours from Planes 2 to 4 (Fig. 2b) before 4320 min when the bitumen recovery almost plateaued. The temperature contours describe the temperature data at the thermocouple

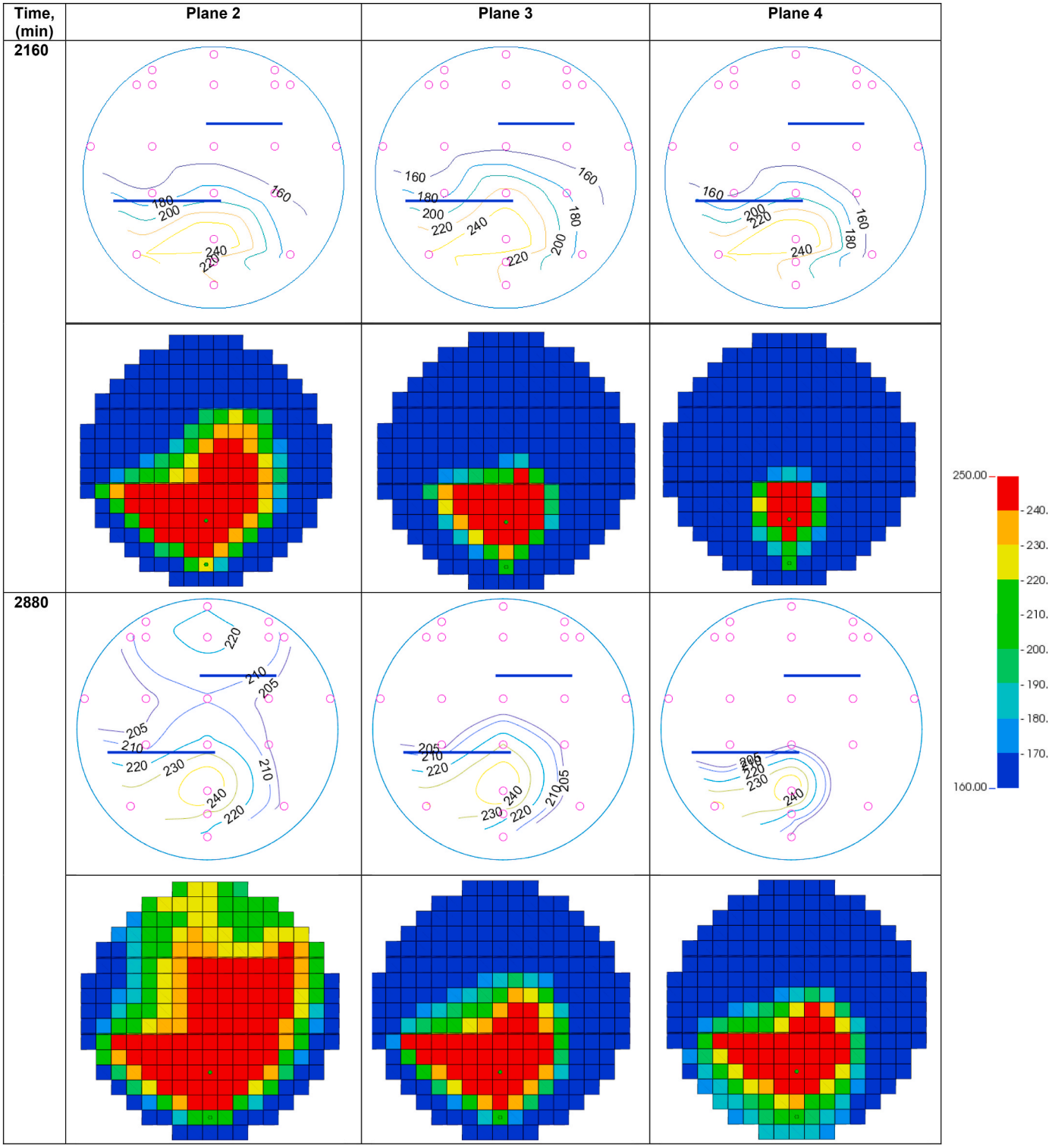

Fig. 6. Temperature profiles on planes 2 to 4 (Fig. 2b) in the SA-SAGD experiment and in the history-matched SA-SAGD simulation.

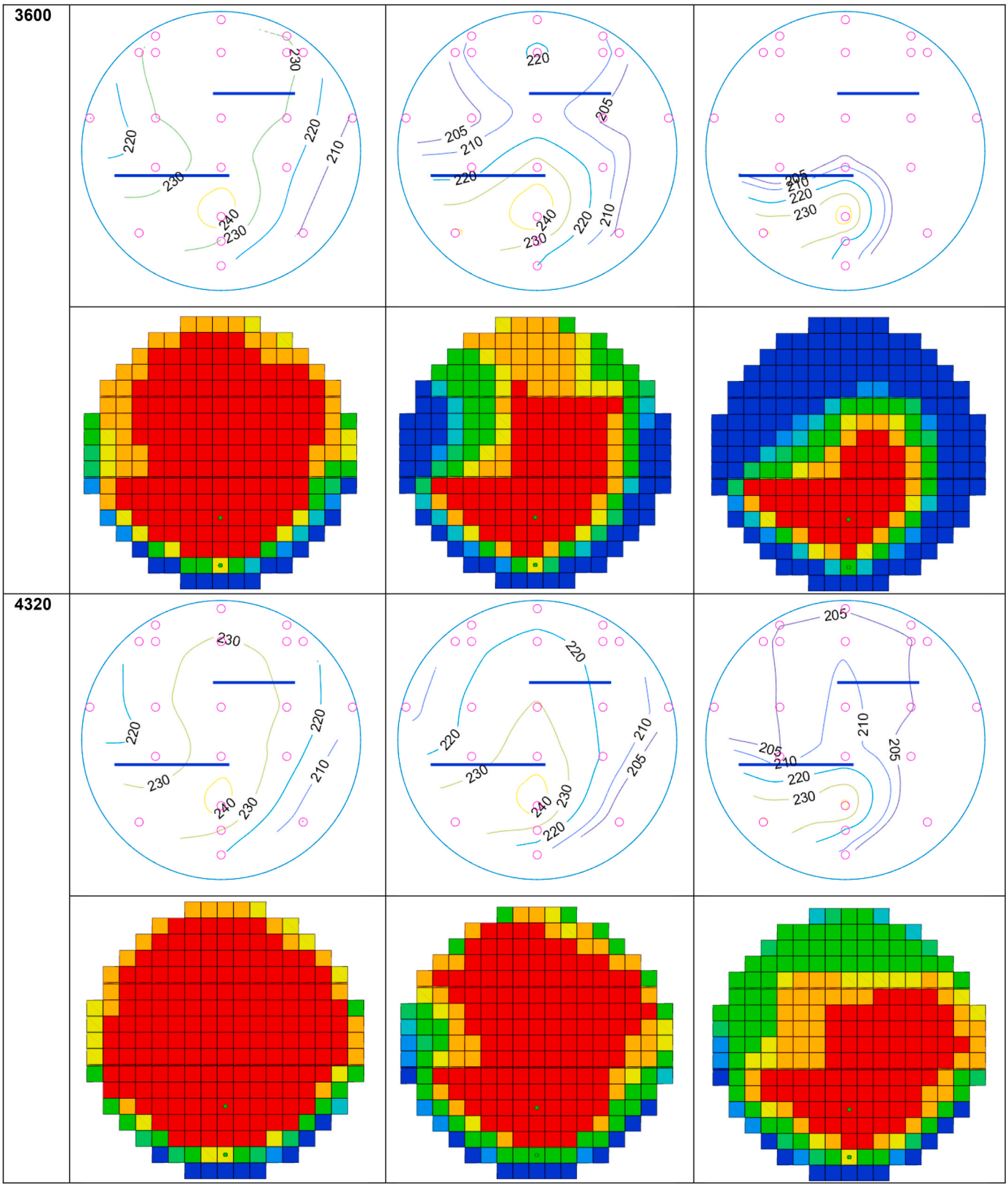

Fig. 6. (*continued*).

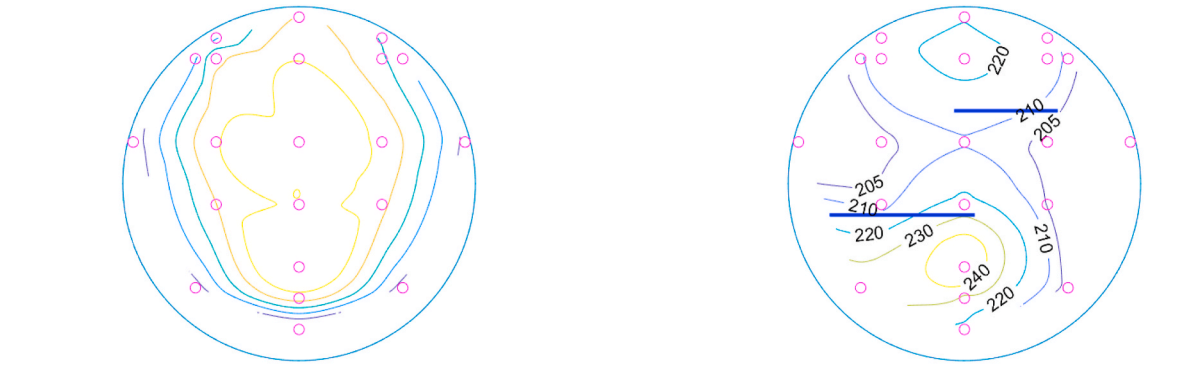

a. Homogeneous sandpack (figure from Sheng et al. [28], temperatures from inside to outside are 240, 225, 210, and 195°C)

b. Heterogeneous sandpack (this research)

Fig. 7. Comparison of temperature distributions in the middle of the sandpack for the homogeneous SA-SAGD experiment (Sheng et al., 2021b) and the heterogeneous SA-SAGD experiment (this research) when bitumen recovery was 20000 cm^3. The chamber expansion above the upper shale plate was indicated by the high-temperature region isolated from another chamber containing the well pair.

locations shown in Fig. 6. The corresponding temperature of each contour line is given in the figure. Planes 1 and 5 are not shown here because they were substantially affected by heat losses to the metal flanges. The temperature contours are useful for history matching to indicate the steam chamber growth in the next section. The steam chamber developed most rapidly in Plane 2, followed by Planes 3 and 4.

Some of the contours in Fig. 6 indicate how a steam chamber expanded from the lower part to the upper part through the tortuous paths (e.g., Plane 2 from 2160 min to 2880 min–3600 min). To highlight the interesting chamber expansion, Fig. 7 compares the temperature profiles in Plane 2 from the current research and from the homogeneous SA-SAGD experiment (Sheng et al., 2021a) when bitumen recovery was 20,000 cm^3. With the homogeneous sandpack (Fig. 7a), the high-temperature zone above 230 °C fully developed to the ceiling of the sandpack. In the heterogeneous sandpack, the temperatures above 230 °C were restrained below the lower shale plate; however, the closure of the 220 °C contour line above the upper shale plate indicated that a steam chamber was emerging. That is, this emerging steam chamber occurred by heat convection (not conduction) from the injection well through the lower-temperature tortuous paths between the shale plates. This should have been possible with components that carried heat without being condensed on the way as confirmed in the history-matched simulation model. Such components included light to intermediate solvent components. This vertical expansion of a steam chamber away from the injection well highlights the importance of volatile components in expanding a steam chamber as reported in Sheng et al. (2021b) for the homogeneous sandpack case.

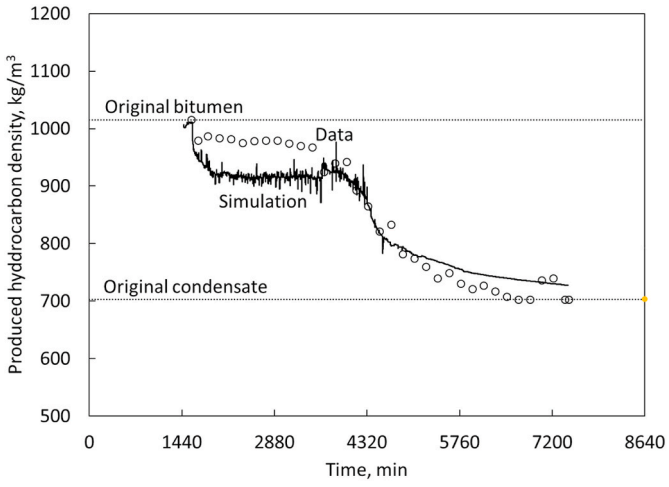

Fig. 8. Produced hydrocarbon densities from the SA-SAGD experiment and the history-matched SA-SAGD simulation.

Fig. 8 shows the densities of produced hydrocarbon after dehydration in reference to the original bitumen and condensate densities at standard conditions. The produced hydrocarbon density gradually decreased from the bitumen density, 1015 kg/m^3, as the steam chamber expanded. The density data before 4320 min indicated the dilution of bitumen by condensate. After 4320 min when the bitumen recovery plateaued, the oil density decreases rapidly and gradually approached the condensate density.

Fig. 9 presents the excavated sandpack after the SA-SAGD experiment. Five locations were sampled from each segment, and the yellow circles in Fig. 9 locate the samples that were successfully taken. Table 1 reports the oil saturations of the successful samples. The photo shows that the color inside the sandpack was light in regions away from shale plates, and the color was darker immediately above and below the shale plates. The clean sand was where the oil was swept by a sufficient amount of solvent to result in a small oil saturation. In contrast, the sand color was darker where the solvent was not easy to condense (near the wellbore), or where shale plates made stagnant/slow flow; e.g., the regions immediately below the upper shale plates in Planes 2 and 3.

During the experiment, the produced dry gas composition was analyzed by gas chromatography. The amount of H_2S production indicates the intensity of aquathermolysis (Ovalles, 2019). The cumulative H_2S production was 0.3 L until the end of the experiment. This amount was similar to the homogeneous SA-SAGD experiment by Sheng et al. (2021b), and was 5 times smaller than the SAGD experiment by Sheng et al. (2020). The reduced level of aquathermolysis was conceivable because the solvent accumulation resulted in lowered steam chamber temperatures and because SA-SAGD experiments were shorter than SAGD with a larger oil production rate.

6. History matching and analysis

6.1. Numerical simulation methods and history matching

The goal of history matching was to calibrate the numerical simulation model to match the injection/production histories and the temperature distributions during the experiment. CMG STARS (Computer Modelling Group, 2018) was used for the history matching.

The history matching consisted of two main steps. The first step was to match the temperature profiles by adjusting the heat losses through thermal properties. The second step was to match the hydrocarbon and

Fig. 9. Photos taken for the excavated sandpack after the SA-SAGD experiment. The pictures in the 1st row are on the injection (heel) end, and the pictures in the 2nd row are on the production (toe) end.

Table 1
Remaining oil saturation in the excavated samples. The asphaltenes contents are not reliably measurable due to low oil saturations in this research.

Layer No.	Sample No.	Oil saturation, %
1	1	3.83
1	3	17.00
1	4	16.10
2	8	5.83
2	9	9.39
2	12	9.59
3	13	1.65
3	15	6.25
3	16	0.21
3	18	6.54
4	19	1.11
4	20	1.83
4	22	3.12
5	27	0.25
5	28	0.00
5	30	0.00
6	31	0.00
6	32	0.00
6	33	0.30
6	34	0.16
7	37	0.10
7	38	0.00
7	41	9.77
7	42	4.33
8	45	0.00
8	46	9.77
8	47	4.33

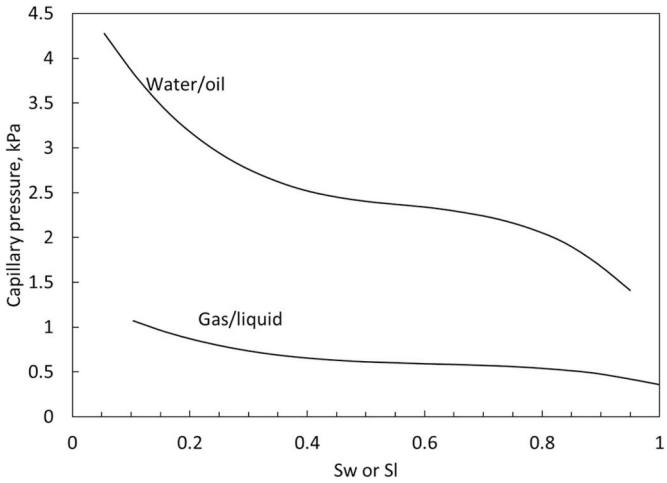

Fig. 10. Capillary pressure model in the SA-SAGD simulation model (Sheng et al., 2021b). The interfacial tensions of oil/water and liquid/gas pairs are 18 dyn/cm, and 4.5 dyn/cm, respectively.

water production histories by using relative permeability parameters. Because of the overlap in carbon number distribution between bitumen and condensate (see Figure A-1), the history-matching used the cumulative produced hydrocarbon weights, instead of separately matching bitumen and condensate volumetric data. Note that the hydrocarbon

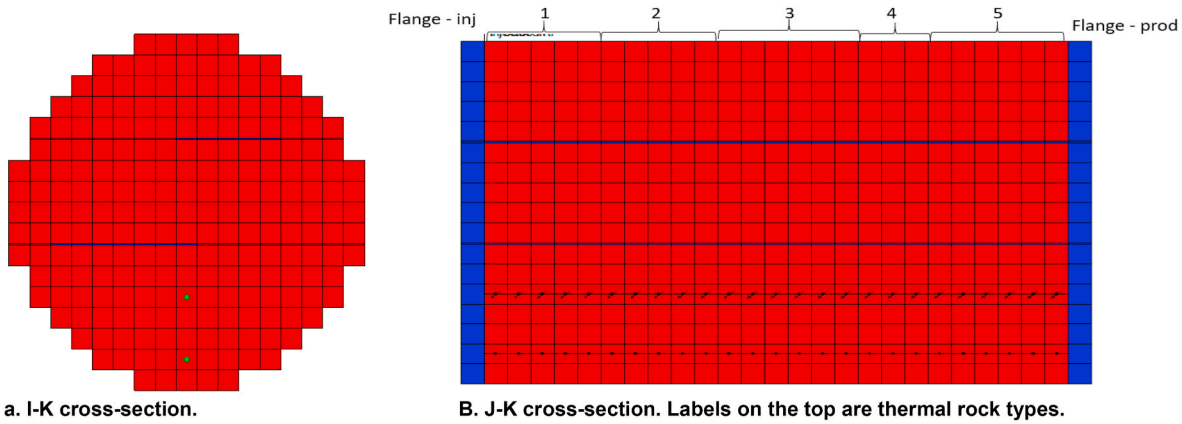

Fig. 11. Numerical reservoir simulation model. Clean sand is in red. Horizontal think bars in blue are shale plates. The production side is on the right, and the injection side is on the left in Fig. 11b.

weights were directly measured in the experiments. Permeability, porosity, and fluid properties were determined by separate experiments and therefore not subject to any adjustment (see the Methods for SA-SAGD Experiment section and Appendix). The capillary pressure from the SA-SAGD experiment by Sheng et al. (2021b) was used for this research because of similar fluid properties and operation conditions (Fig. 10).

Fig. 11 shows the cross-sections of the sandpack model. There were 19 gridblocks in the I direction, 27 gridblocks in the J direction (along the wellbore), and 19 gridblocks in the K (vertical) direction. The shale plates were modeled by two thin layers with petrophysical properties of flow barriers. The shale gridblock had the dimensions of 0.025 m × 0.0488 m × 0.008 m (I × J × K). The thickness for the layer immediately above shale plates was 0.017 m, and for other layers, the thickness was 0.025 m.

The fluid model contained three condensate pseudocomponents (S1, S2, and S3) and two bitumen pseudocomponents (B1 and B2). S1, S2, and S3 respectively resembled C_4, C_7, and C_{21} in terms of volatility. B1 and B2 represented a distillable and a non-distillable bitumen component, respectively. The fluid models were made by using the Peng-Robinson equation of state (PR EOS) along with fluids data, such as carbon number distribution of bitumen and condensates, molecular weights, densities, and PVT experimental data (Appendix A). Appendix also provides the viscosity and density model used for this research.

During the history matching, the thermal conductivities were fixed to 1.23, 0.36, 0.072, and 0.02 J/(cm min °C) for the sand, water, oil, and gas phases, respectively. The uneven steam chamber growth along the wellbore in Fig. 6 required different sets of thermal parameters in the J direction. Seven sets of thermal parameters were considered in history matching, as given in Table 2. Fig. 11 shows the corresponding locations of each thermal rock type. Additionally, skin factors (Table 2) for the injection well were used to mechanistically reproduce the non-uniform injection of steam along the injection well, which resulted in the chamber growth patterns shown in Fig. 6. The skin factors were made inactive at 3600 min when the steam chamber was able to develop throughout the sandpack.

Fig. 12 shows the relative permeability curves for the best match of temperature and hydrocarbon recovery. Table 3 shows the corresponding Corey's model parameters. The permeability curves were similar to those presented in Sheng et al. (2021b), except that the gas relative permeability in this research was 40% smaller.

Figs. 3 and 4 compare the injection and production histories of hydrocarbon and water in the experiment and the calibrated simulation model. The total hydrocarbon production and water injection/production histories were reasonably matched. Fig. 6 presents the temperature matching up to three days when the bitumen recovery plateaued. The temperature profiles were reasonably captured with the numerical simulation. Fig. 8 shows that the simulation was able to capture the compositional variation in the produced hydrocarbon.

6.2. Analysis

Understanding the impact of permeability barriers would require two SA-SAGD experiments with/without the permeability barriers with all other static/dynamic conditions being set identical. However, many factors (technical/non-technical) that evolved throughout the multi-year research made it difficult; for example, the injection rates were different between this research and the previous ones. One way to analyze the impacts of the shale plates was to perform a numerical experiment without using the shale plates based on the calibrated simulation model. This section compares two simulations, the calibrated simulation in the previous section (i.e., the "calibrated case") and the hypothetically homogeneous case based on the calibrated model (i.e., the "homogenized case"). The two simulation results were compared in

Table 2
Thermal parameters for the history-matched SA-SAGD simulation. I, J and +K and -K represent the coordinate system in the simulation, representing the directions perpendicular to the well pair, parallel to the well pair, below and above the sandpacks, respectively.

	Flange – Injection end	Flange – Production end	Sandpack 1	Sandpack 2	Sandpack 3	Sandpack 4	Sandpack 5
Thermal conductivity in I, J/(cm min °C)	–	–	4.0	4.0	4.0	4.0	0.0
Heat capacity in I, J/(cm^3 °C)	–	–	2.0	1.0	1.0	1.0	0.0
Thermal conductivity in J, J/(cm min °C)	0.05	0.2	–	–	–	–	–
Heat capacity in J, J/(cm^3 °C)	0.25	0.02	–	–	–	–	–
Thermal conductivity in +K, J/(cm min °C)	0.03	0.20	8.0	10.0	8.0	8.0	0.1
Heat capacity in +K, J/(cm^3 °C)	0.02	0.02	4.0	6.0	4.0	4.0	0.02
Thermal conductivity in -K, J/(cm min °C)	0.02	0.15	0.0	3.0	4.0	4.0	0.0
Heat capacity in -K, J/(cm^3 °C)	0.02	0.02	0.0	0.8	1.0	1.0	0.0
Skin factor for injection in this section	–	–	0	30	30	200	200

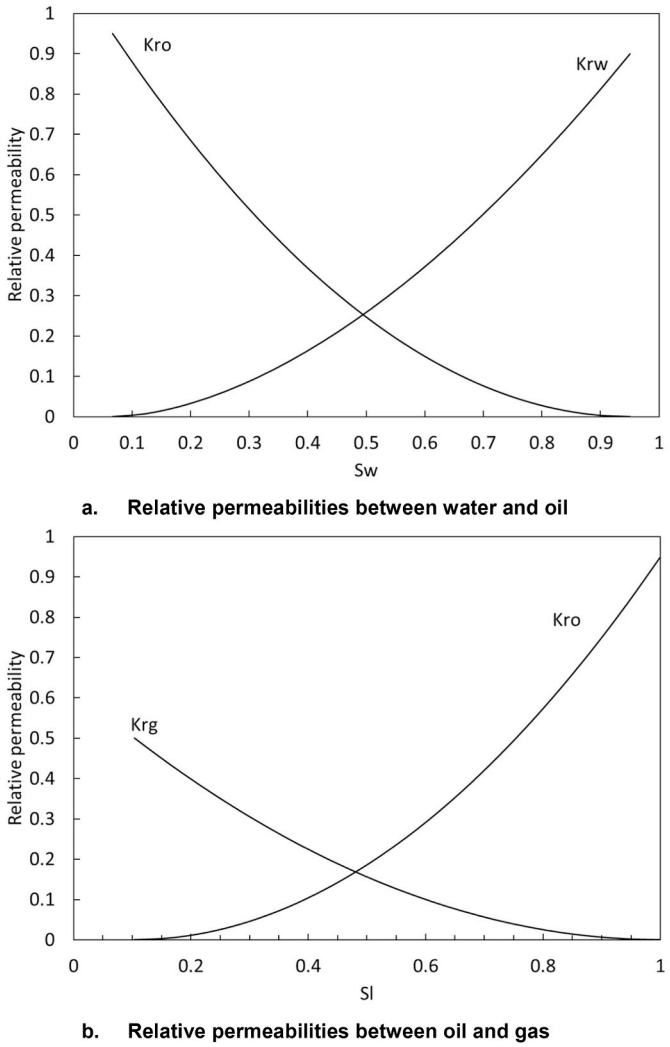

Fig. 12. Relative permeability models for the history-matched SA-SAGD simulation model.

Table 3
Relative permeability parameters for the history-matched SA-SAGD simulation.

Parameters	Values
S_{wr}	0.054
S_{or}	0.050
S_{gr}	0
K_{ro}	0.95
K_{rw}	0.90
K_{rg}	0.50
K_{rw} exponent	1.75
K_{ro} exponent	2.0
K_{rg} exponent	2.0

terms of the bulk performance, such as SOR and oil recovery, and the compositional impact on the condensate and produced bitumen.

Fig. 13 shows that the cumulative SOR was approximately 1.7 cm^3/cm^3 for the hypothetically homogeneous case and 2.5 cm^3/cm^3 for the calibrated simulation case at the main bitumen production periods. Although this is a numerical comparison, the results are consistent with the experimental results shown in Fig. 5, in which the shale plates increased the SOR by 0.5 cm^3/cm^3 from the homogeneous SA-SAGD experiment.

Since the steam and solvent coinjection rates were the same for the

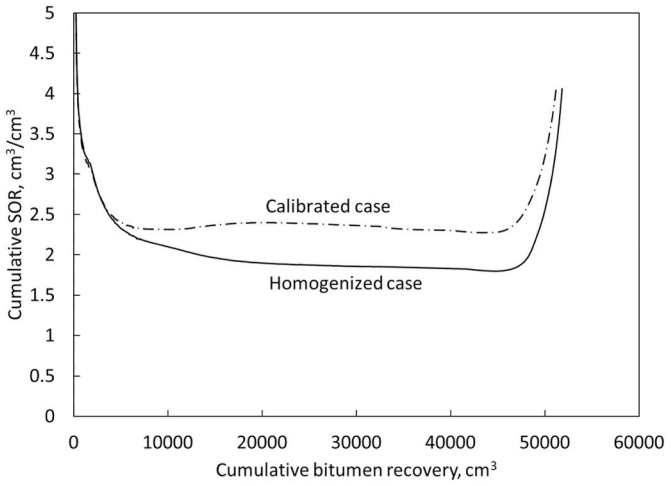

Fig. 13. Cumulative SOR of SA-SAGD using the calibrated simulation model based on the experimental results in this research ("calibrated case") and using the hypothetically homogeneous case based on the calibrated model ("homogenized case").

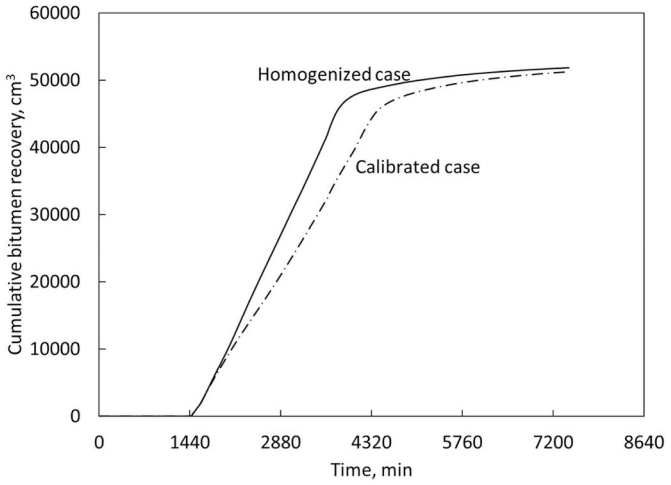

Fig. 14. Cumulative bitumen recovery for SA-SAGD using the calibrated simulation model based on the experimental results in this research ("calibrated case") and using the hypothetically homogeneous case based on the calibrated model ("homogenized case").

two simulation cases, the bitumen recoveries were conveniently compared on the same basis for the impact of the shale plates on the SOR. Fig. 14 shows that the shale plates slowed down the bitumen production rate by 25%, leading to systematically smaller oil recoveries than the hypothetically homogeneous case.

Fig. 15a shows the oil saturation distribution on Plane 3 (in the middle of the sandpack) when the bitumen recovery was 30000 cm^3. The oil flow rate was also marked out in this figure on the log scale. The length of the arrow represents the magnitude of the oil flow rate, and the direction shows the oil flow direction. The oil flowed mainly in the vertical direction towards the producer in the homogeneous case. In the heterogeneous case, the shale plates served as barriers that divert the oil flow from the vertical to horizontal direction near the shale plates, making the oil flow paths tortuous. The tortuous flow increased the time for the oil to reach the producer, and therefore delayed the oil production. Fig. 15b shows the S2 concentration in the oil phase when bitumen recovery was 30000 cm^3. The accumulation of solvent was observed in slow-flow regions near the permeability barriers, which was also

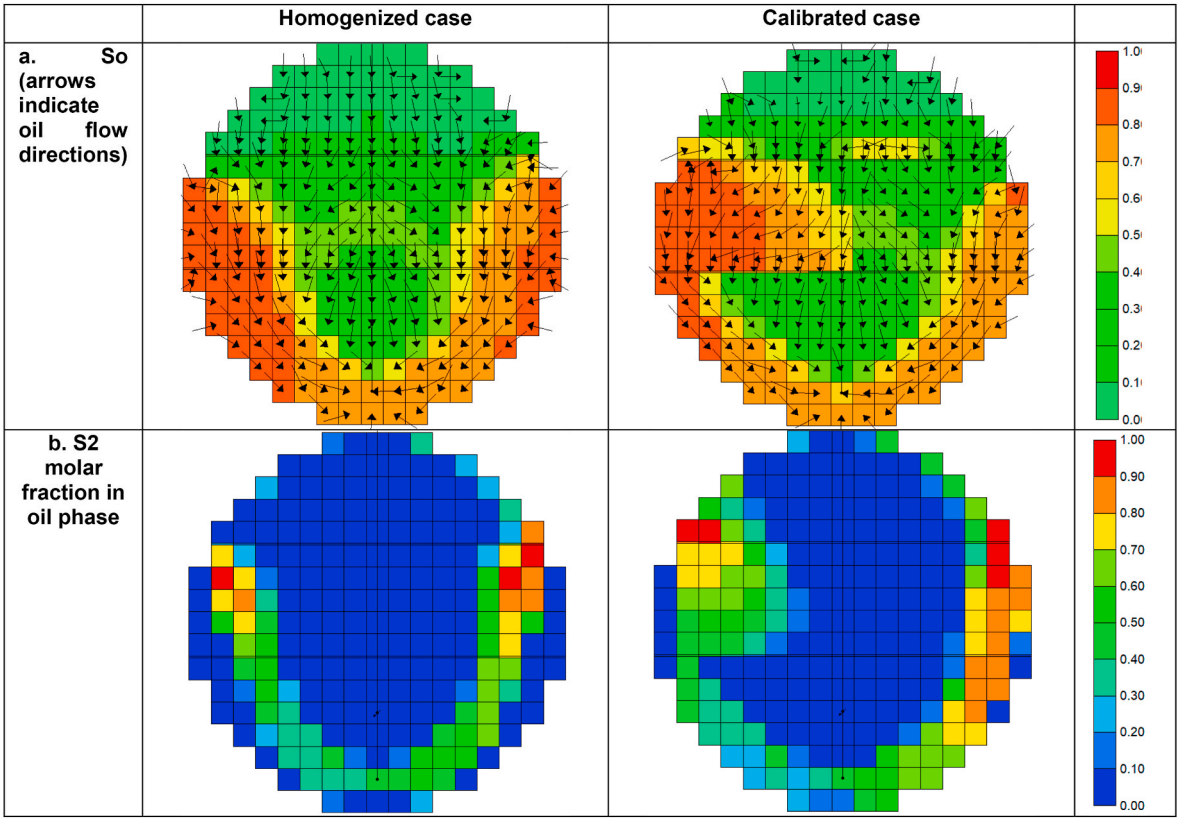

Fig. 15. Simulated profiles of SA-SAGD in SAGD in homogenized and calibrated numerical simulation cases when bitumen production was 30000 cm^3. The calibrated case was based on the experimental results. The homogenized case was made by removing the shale plates from the calibrated simulation model.

reported by Venkatramani and Okuno (2018a). The accumulation of solvent enhanced the mobility of bitumen components that would otherwise stay stagnant near the permeability barriers.

Fig. 16a shows the total solvent accumulation for the two cases in the sandpack, and Fig. 16bc show the solvent accumulation inside and outside the steam chamber, respectively. The cumulative solvent amount in Fig. 16a contains the amount of solvent inside and outside the steam chamber in Fig. 16bc. The total solvent retention in the calibrated simulation case was approximately 15% higher than in the other case. The tortuous and slower oil flow paths resulted in a longer residence time of solvent, causing the solvent components to accumulate in the sandpack. A larger amount of solvent was present both inside and outside of the steam chamber in the calibrated simulation case. The solvent accumulation inside the steam chamber enabled the chamber to expand at lower temperatures (than the steam temperature) while suppressing excessive heat losses to the surroundings. The solvent outside the chamber indicates the dilution of bitumen. These results mechanistically illustrate that the increased retention of solvent (Fig. 16) contributed to the effectiveness of SA-SAGD in the presence of shale plates.

Fig. 17a compares the produced bitumen density in the two simulation cases at different cumulative bitumen recoveries. The produced bitumen in the hypothetically homogeneous case was overall lighter than in the calibrated simulation case. The difference in produced bitumen density comes from the different produced bitumen compositions. Fig. 17b shows the distillable component (B1) mole percentage in the produced bitumen. The homogeneous case resulted in produced bitumen being 1–2 mol% richer in B1. These results confirm the observations by Sheng et al. (2021b) in their field-scale 3D heterogeneous reservoir simulations. That is, tortuous flow paths enhanced the oil/solvent mixing and reduced the separation of components. The accumulation of solvent reduces the steam chamber temperature, and therefore tends to suppress the vaporization of distillable components in the residual oil.

The simulation results at the end of the experiment were analyzed to understand the excavated sandpack in Fig. 9. Fig. 18 shows the profiles of the simulated overall B2 concentration and oil saturation at the end of the experiment on Plane 2. The overall B2 concentration was a good indicator of the sandpack color because B2 was characterized as a heavy non-distillable component. Results show that the B2 concentration was high immediately above the lower shale plate. The region with the highest B2 concentration occurred between the two shale plates. This is in good agreement with the dark color on Plane 2 between the shale plates (Fig. 9). The dark regions in the sandpack indicate that the oil was not swept sufficiently by the condensate because the two horizontally parallel shale plates made a slow flow region and/or because the condensate accumulation was not sufficient owing to high temperature.

7. Conclusions

This paper presented an SA-SAGD experiment with condensate (a multicomponent hydrocarbon solvent) in a sandpack with two horizontal shale plates in it. The sandpack had a pore volume of 58.7 L. The shale plates placed above the injection well caused tortuous flow paths in the experiment. The SA-SAGD experiment injected a mixture of 2.8 mol% condensate and 98.2 mol% water (35 cm^3/min of water, cold-water equivalent) at 3500 kPa. The material balance of water, bitumen, and condensate and the temperature profiles from the experimental data were history-matched by a numerical simulation model. The calibrated simulation model was used to understand the impact of

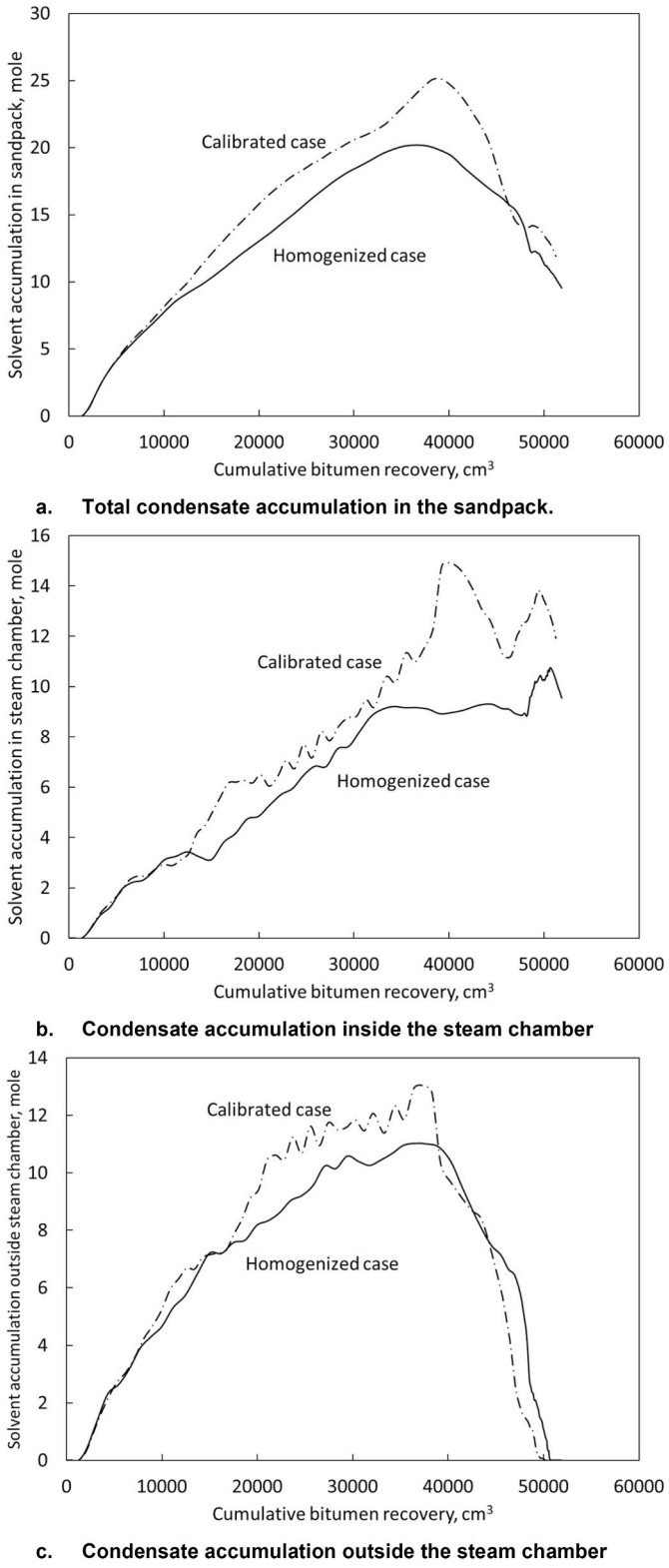

Fig. 16. Condensate accumulation in SA-SAGD in homogenized and calibrated simulation cases. The calibrated case was based on the experimental results. The homogenized case was made by removing the shale plates from the calibrated simulation model.

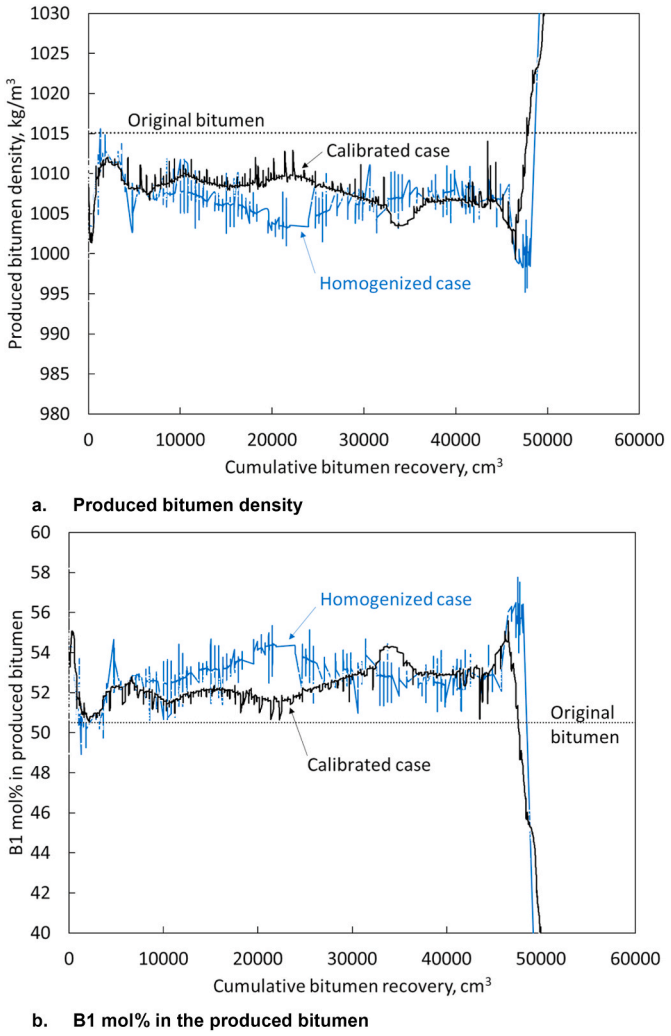

Fig. 17. Produced bitumen properties for SA-SAGD in the homogenized and calibrated simulation cases. The calibrated case was based on the experimental results. The homogenized case was made by removing the shale plates from the calibrated simulation model.

the shale plates on the in-situ flow characteristics. The main conclusions from this experiment and modeling study are as follows:

- Cumulative SOR for the SA-SAGD experiment in the heterogeneous sandpack (this research) was 2–3 cm^3/cm^3 smaller than that of the previous SAGD experiment in the homogeneous sandpack (Sheng et al., 2020), and 0.5 cm^3/cm^3 greater than the SA-SAGD experiment in the homogeneous sandpack (Sheng et al., 2021b). These results indicated that the shale plates increased the cumulative SOR by approximately 25% from the homogeneous SA-SAGD.
- The temperature profiles indicated that the steam chamber vertically expanded from the lower part to the upper part through the tortuous paths at temperatures lower than the steam temperature. The vertical expansion was greatly assisted by an emerging steam chamber above the shale plates, which occurred by convective heat from the injection well through lower-temperature flow paths between shale plates. Because of their volatility, solvent components enabled the steam chamber to expand away from the injection well. To our knowledge, this is the first experimental observation regarding the

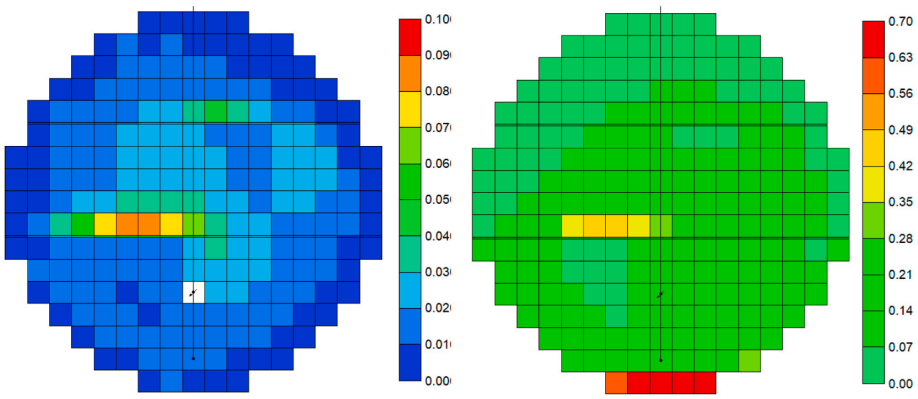

Fig. 18. B2 mole fraction (left) and oil saturation (right) in the calibrated SA-SAGD simulation with the heterogeneous sandpack at the end of the experiment.

important role of volatile solvent components in the growth of a steam chamber under heterogeneity.

- The SA-SAGD experiment in this research resulted in the amount of H_2S production similar to the previous SA-SAGD experiment using the homogeneous sandpack. It was five times lower than that of the SAGD experiment using the homogeneous sandpack. The reduced level of aquathermolysis in SA-SAGD with/without shale plates was likely because the solvent accumulation resulted in lower steam chamber temperatures and because the SA-SAGD experiments were shorter with more rapid oil production than the SAGD experiment.
- The tortuous flow path in this research also resulted in a longer solvent residence time and therefore a greater accumulation of solvent. Material balance analysis showed that the solvent accumulation was 15% greater in the calibrated simulation case than in the hypothetically homogeneous case. The solvent accumulation reduced the solvent temperature and diluted the bitumen where the oil-phase flow was slow.
- The calibrated SA-SAGD simulation case produced denser bitumen than the hypothetically homogeneous case; that is, the produced bitumen density was close to the original bitumen density with the shale plates in the sandpack. Enhanced mixing due to tortuous flow paths reduced the separation of components. The accumulation of solvent reduced the steam chamber temperature, and therefore suppressed the vaporization of distillable components in the residual oil.

Credit author statement

Kai Sheng: Data curation; Formal analysis; Investigation; Methodology; Validation; Visualization; Writing – original draft. Ryosuke Okuno: Conceptualization; Formal analysis; Funding acquisition; Investigation; Methodology; Project administration; Resources; Supervision; Validation; Writing – original draft. Abdullah Al-Gawfi: Data curation; Formal analysis; Investigation; Methodology; Validation; Writing – review & editing. Petro Nakutnyy: Data curation; Formal analysis; Investigation; Methodology; Validation; Writing – review & editing

Declaration of competing interest

The authors declare that they have no known competing financial interests or personal relationships that could have appeared to influence the work reported in this paper.

Data availability

Data will be made available on request.

Acknowledgments

Ryosuke Okuno holds the Pioneer Corporation Faculty Fellowship in the Hildebrand Department of Petroleum and Geosystems Engineering at The University of Texas at Austin. We acknowledge sponsors of the Energi Simulation Industrial Affiliate Program on Carbon Utilization and Storage (ES Carbon UT) at the Center for Subsurface Energy and The Environment at the University of Texas at Austin.

Appendix A. Fluid Modeling in Numerical Simulation

The fluids model used for numerical simulation in STARS (Computer Modelling Group, 2018) is presented here. The bitumen used in this research was characterized by following Kumar and Okuno's method (Kumar and Okuno, 2016) based on the bitumen carbon number distribution (Figure A1) and the bubble points measured for bitumen/synthetic condensate mixtures as presented in Sheng et al. (2021b). The bitumen was characterized by two components, B1 and B2. The former represents a distillable component, and the latter a non-distillable component. Table A1 gives the resulting EOS model.

The solvent used in this paper was a condensate with the carbon number distribution given in Figure A1. The components were grouped into three components (S1, S2, and S3), of which the average carbon numbers were 4, 8, and 21, respectively. This grouping scheme was used also by Sheng et al. (2021a), and the critical properties for the condensate pseudocomponents are given in Table A1. The condensate and the bitumen share the carbon number range between C_8 and C_{60}, as described in "Experimental Results and Discussion."

In STARS (2018), the oil-phase densities are modeled assuming the ideal mixing; that is

$$1/\rho_L = \sum_{i=1}^{Nc} x_{iL}/\rho_{iL} \tag{A-1}$$

where ρ_L is the molar density of oil phase, x_{iL} the mole fraction of component i in the oil phase, and N_C is the number of components. ρ_{iL} is the molar density of each component modeled as

$$\rho_{iL} = \rho_{iref} \exp\left[-\alpha_1 (T - T_{ref}) - \frac{1}{2}\alpha_2 (T^2 - T_{ref}{}^2) + \alpha_3 (P - P_{ref}) + \alpha_4 (P - P_{ref})(T - T_{ref}) \right] \quad \text{(A-2)}$$

where P_{ref} and T_{ref} are the reference pressure and temperature, 101.3 kPa and 15.56 °C. ρ_{iref} is the molar density of component i at these conditions. The α coefficients and ρ_{iref} are adjustment parameters. Table A2 shows the bitumen and solvent component density models. Initially, the closest alkane properties were used for each pseudocomponents. Then, the parameters were perturbed to match the bitumen densities at 3500 kPa (Table A3), and the condensate density at standard conditions, 703 kg/m^3.

The oil viscosities are modeled in STARS using the weighted log-linear mixing of pure components

$$\ln \mu_L = \sum_{i=1}^{Nc} q_i x_i \ln \mu_i = \sum_{i=1}^{Nc} f_i \ln \mu_i \quad \text{(A-3)}$$

where μ_L is the oil phase viscosity. μ_i, q_i and x_i are the viscosity, scaling factor and molar fraction of component i, respectively. The summation of $q_i x_i$ for all the components should be 1.0. B2 was set as the key component, and the f_{B2} table was given to STARS. Because of the similarity of the condensate of this paper to the one in Sheng et al. (2021a), their condensate models were implemented in this research. The bitumen viscosity model was calibrated by assuming a log-linear mixing of components based on data in Table A4. The resulting STARS viscosity inputs are given in Table A5.

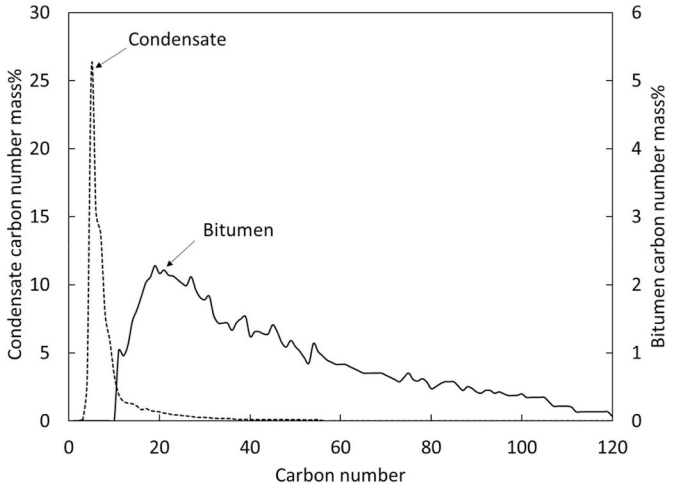

Fig. A1. Carbon number distribution of condensate and bitumen.

Table A1
Calibrated PR EOS model used in the simulations with CMG STARS (Computer Modelling Group, 2018). Water solubility in oil was neglected.

a. Compositions, critical properties, acentric factors, and molar mass for hydrocarbon pseudocomponents

Component	Mol%	MW, g/mol	Tc, °C	Pc, kPa	Acentric factor
Condensate					
S1	5.26	57.4	149.37	3766	0.2477
S2	92.94	93.2	281.60	3085	0.0899
S3	1.80	407.6	665.09	1325	0.4158
Dead Bitumen					
B1	49.5	283.0	526.35	2000	0.3996
B2	50.5	831.1	976.62	1314	0.8712

b. Interaction parameters in PR EOS

	S1	S2	S3	B1	B2
S1	0				
S2	0.0291	0			
S3	0.0720	0	0		
B1	0.0642	0	0	0	
B2	0.0843	0	0	0	0

Table A2
Density models used for components.

	S1	S2	S3	B1	B2
ρ_{ref}, kg/m^3	585.6	687.6	1078.26	836.00	1092.08
CP, kPa^{-1}	3.58×10^{-6}	3.02×10^{-6}	7.7×10^{-7}	9.47×10^{-7}	6.71×10^{-8}
CT1, °C $^{-1}$	5.18×10^{-5}	6.06×10^{-5}	3.19×10^{-4}	1.50×10^{-4}	6.34×10^{-4}
CT2, °C $^{-2}$	5.05×10^{-6}	4.20×10^{-6}	2.53×10^{-6}	1.12×10^{-6}	7.48×10^{-8}
CPT, kPa^{-1}°C $^{-1}$	4.56×10^{-8}	4.56×10^{-9}	-1.38×10^{-9}	4.16×10^{-9}	2.17×10^{-10}

Table A3
Measured bitumen densities.

Pressure, kPa	Temperature, °C						
	66.5	81.0	100.0	119.9	151.0	170.9	199.3
1002	982.79	974.76	963.25	949.70	929.92	916.95	N/A
2002	983.35	975.48	963.88	950.49	930.78	917.85	899.41
4001	984.59	976.72	965.32	951.94	932.47	919.77	901.53
6003	985.67	977.86	966.64	953.37	934.15	921.49	903.58
8004	986.73	979.02	967.90	954.75	935.74	923.23	905.54
9999	987.85	980.26	969.20	956.17	937.26	924.99	907.41

Table A4
Measured bitumen viscosities.

Pressure, kPa	Temperature, °C						
	58.9	64.7	79.4	98.9	119.5	149.9	169.2
1003	4599	2526	988.2	224.4	79.51	27.89	N/A
2003	4798	2644	1017	235.4	82.33	29.03	15.92
4002	5082	2850	1102	247.4	85.68	30.23	16.87
6001	5394	2986	1161	267.2	90.04	31.42	17.81
8001	5851	3203	1221	273.3	94.87	N/A	N/A
10001	6055	3397	1304	283.5	98.82	N/A	N/A

Table A5
Viscosity model for CMG STARS (Computer Modelling Group, 2018).

a. Viscosity table for pure components					
T, °C	S1	S2	S3	B1	B2
10	1.9114×10^{-1}	6.3089×10^{-1}	1.1862	1.9718	1.6558×10^{12}
20	1.7017×10^{-1}	5.6456×10^{-1}	1.0848	1.3152	4.7605×10^{-10}
30	1.5150×10^{-1}	5.0520×10^{-1}	9.9174×10^{-1}	9.2504	2.4269×10^{9}
40	1.3488×10^{-1}	4.5208×10^{-1}	9.0680×10^{-1}	6.7937	1.9713×10^{8}
50	1.2008×10^{-1}	4.0454×10^{-1}	8.2914×10^{-1}	5.1701	2.3445×10^{7}
60	1.0690×10^{-1}	3.6201×10^{-1}	7.5814×10^{-1}	4.0522	3.8177×10^{6}
70	9.5171×10^{-2}	3.2395×10^{-1}	6.9321×10^{-1}	3.2555	8.0656×10^{5}
80	8.4729×10^{-2}	2.8988×10^{-1}	6.3384×10^{-1}	2.6705	2.1169×10^{5}
90	7.5432×10^{-2}	2.5940×10^{-1}	5.7956×10^{-1}	2.2299	6.6640×10^{4}
100	6.7156×10^{-2}	2.3213×10^{-1}	5.2993×10^{-1}	1.8906	2.4447×10^{4}
110	5.9787×10^{-2}	2.0772×10^{-1}	4.8454×10^{-1}	1.6243	1.0208×10^{4}
120	5.3227×10^{-2}	1.8588×10^{-1}	4.4305×10^{-1}	1.4117	4.7583×10^{3}
130	4.7387×10^{-2}	1.6634×10^{-1}	4.0510×10^{-1}	1.2395	2.4362×10^{3}

(*continued on next page*)

Table A5 (*continued*)

a. Viscosity table for pure components

T, °C	S1	S2	S3	B1	B2
140	4.2187×10^{-2}	1.4885×10^{-1}	3.7041×10^{-1}	1.0981	1.3517×10^{3}
150	3.7558×10^{-2}	1.3320×10^{-1}	3.3869×10^{-1}	9.8076×10^{-1}	8.0368×10^{2}
160	3.3437×10^{-2}	1.1919×10^{-1}	3.0968×10^{-1}	8.8227×10^{-1}	5.0722×10^{2}
170	2.9768×10^{-2}	1.0666×10^{-1}	2.8316×10^{-1}	7.9886×10^{-1}	3.3709×10^{2}
180	2.6502×10^{-2}	9.5445×10^{-2}	2.5891×10^{-1}	7.2763×10^{-1}	2.3431×10^{2}
190	2.3594×10^{-2}	8.5410×10^{-2}	2.3674×10^{-1}	6.6632×10^{-1}	1.6937×10^{2}
200	2.1005×10^{-2}	7.6429×10^{-2}	2.1646×10^{-1}	6.1319×10^{-1}	1.2669×10^{2}
210	1.8701×10^{-2}	6.8393×10^{-2}	1.9793×10^{-1}	5.6686×10^{-1}	97.645
220	1.6649×10^{-2}	6.1202×10^{-2}	1.8098×10^{-1}	5.2622×10^{-1}	77.271
230	1.4822×10^{-2}	5.4767×10^{-2}	1.6548×10^{-1}	4.9038×10^{-1}	62.586
240	1.3196×10^{-2}	4.9009×10^{-2}	1.5130×10^{-1}	4.5861×10^{-1}	51.743
250	1.1748×10^{-2}	4.3856×10^{-2}	1.3835×10^{-1}	4.3033×10^{-1}	43.564
260	1.0459×10^{-2}	3.9244×10^{-2}	1.2650×10^{-1}	4.0504×10^{-1}	37.275
270	9.3112×10^{-3}	3.5118×10^{-2}	1.1567×10^{-1}	3.8233×10^{-1}	32.356
280	8.2896×10^{-3}	3.1426×10^{-2}	1.0576×10^{-1}	3.6187×10^{-1}	28.449
290	7.3800×10^{-3}	2.8121×10^{-2}	9.6703×10^{-2}	3.4336×10^{-1}	25.301

b. Scaling factor (f_{B2}) - composition table for the viscosity model.

Mole fraction	f_{B2}
0	0.0000
0.1	0.1679
0.2	0.2508
0.3	0.3136
0.4	0.4020
0.5	0.5002
0.6	0.6000
0.7	0.7000
0.8	0.8000
0.9	0.9000
1	1.0000

References

Al-Murayri, M.T., Maini, B.B., Harding, T.G., Oskouei, J., 2016a. Cracked naphtha coinjection in steam-assisted gravity drainage. Energy Fuel. 30 (7), 5330–5340. https://doi.org/10.1021/acs.energyfuels.5b02773.

Al-Murayri, M.T., Maini, B.B., Harding, T.G., Oskouei, J., 2016b. Multicomponent solvent Co-injection with steam in heavy and extra-heavy oil reservoirs. Energy Fuel. 30 (4), 2604–2616. https://doi.org/10.1021/acs.energyfuels.5b02774.

Ayodele, O.R., Nasr, T.N., Beaulieu, G., Heck, G., 2009. Laboratory experimental testing and development of an efficient low pressure ES-SAGD process. J. Can. Petrol. Technol. 48 (9), 54–61. https://doi.org/10.2118/09-09-54, 0.

Computer Modelling Group, 2018. STARS Version 2018 User's Guide. Computer Modelling Group, Calgary, Alberta, Canada.

Deng, X., Huang, H., Zhao, L., Law, D.S., Nasr, T.N., 2010. Simulating the ES-SAGD process with solvent mixture in Athabasca reservoirs. J. Can. Petrol. Technol. 49 (1), 38–46. https://doi.org/10.2118/132488-PA, 0.

Dong, L., 2012. Effect of vapour–liquid phase behaviour of steam–light hydrocarbon systems on steam assisted gravity drainage process for bitumen recovery. Fuel 95, 159–168. https://doi.org/10.1016/j.fuel.2011.10.044.

Gotawala, D.R., Gates, I.D., 2010. On the impact of permeability heterogeneity on SAGD steam chamber growth. Nat. Resour. Res. 19 (2), 151–164. https://doi.org/10.1007/s11053-010-9114-0.

Hosseininejad Mohebati, M., Maini, B.B., Harding, T.G., 2012. Experimental investigation of the effect of hexane on SAGD performance at different operating pressures. In: SPE Heavy Oil Conference Canada. Society of Petroleum Engineers. https://doi.org/10.2118/158498-MS.

Huang, S., Yang, L., Xia, Y., Du, M., Yang, Y., 2019. An experimental and numerical study of a steam chamber and production characteristics of SAGD considering multiple barrier layers. J. Petrol. Sci. Eng. 180, 716–726. https://doi.org/10.1016/j.petrol.2019.05.062.

Jha, R.K., Kumar, M., Benson, I., Hanzlik, E., 2013. New insights into steam/solvent-coinjection-process mechanism. SPE J. 18 (5), 867–877. https://doi.org/10.2118/159277-PA, 0.

Keshavarz, M., Okuno, R., Babadagli, T., 2014. Efficient oil displacement near the chamber edge in ES-SAGD. J. Petrol. Sci. Eng. 118, 99–113. https://doi.org/10.1016/j.petrol.2014.04.007.

Keshavarz, M., Okuno, R., Babadagli, T., 2015. Optimal application conditions for steam/solvent coinjection. SPE Reservoir Eval. Eng. 18 (1), 20–38. https://doi.org/10.2118/165471-PA.

Khaledi, R.R., Beckman, M.S., Pustanyk, K., Mohan, A., Wattenbarger, C.C., Dickson, J.L., Boone, T.T., 2012. Physical modeling of solvent-assisted SAGD. In: SPE Heavy Oil Conference Canada. Society of Petroleum Engineers. https://doi.org/10.2118/150676-MS.

Khaledi, R.R., Boone, T.J., Motahhari, H.R., Subramanian, G., 2015. Optimized solvent for solvent assisted-steam assisted gravity drainage (SA-SAGD) recovery process. In: SPE Canada Heavy Oil Technical Conference. Society of Petroleum Engineers. https://doi.org/10.2118/174429-MS.

Kumar, A., Hassanzadeh, H., 2021a. A qualitative study of the impact of random shale barriers on SAGD performance using data analytics and machine learning. J. Petrol. Sci. Eng. 205, 108950 https://doi.org/10.1016/j.petrol.2021.108950.

Kumar, A., Hassanzadeh, H., 2021b. Impact of shale barriers on performance of SAGD and ES-SAGD—a review. Fuel 289, 119850. https://doi.org/10.1016/j.fuel.2020.119850.

Kumar, A., Okuno, R., 2016. A new algorithm for multiphase fluid characterization for solvent injection. SPE J. 21 (5), 1688–1704. https://doi.org/10.2118/175123-PA, 0.

Ma, Z., Leung, J.Y., 2020. Integration of deep learning and data analytics for SAGD temperature and production analysis. Comput. Geosci. 24 (3), 1239–1255. https://doi.org/10.1007/s10596-020-09940-x.

Nasr, T.N., Beaulieu, G., Golbeck, H., Heck, G., 2003. Novel expanding solvent-SAGD process "ES-SAGD". J. Can. Petrol. Technol. 42 (1), 13–16. https://doi.org/10.2118/03-01-TN.

Ovalles, C., 2019. Subsurface Upgrading of Heavy Crude Oils and Bitumen. CRC Press.

Prats, M., 1982. Thermal Recovery, vol. 7. SPE Monograph Series, ISBN 978-1-61399-548-8.

Shen, C., 2013. Enhanced Oil Recovery Field Case Studies, first ed. Elsevier, pp. 413–455 (Chapter 13).

Sheng, K., Okuno, R., Wang, M., 2018. Dimethyl ether as an additive to steam for improved steam-assisted gravity drainage. SPE J. 23 (4), 1201–1222. https://doi.org/10.2118/184983-PA.

Sheng, K., Okuno, R., Imran, M., Yamada, T., 2020. An experimental study of steam-assisted gravity drainage. Accepted for publication in *SPE Journal*. https://doi.org/10.2118/200867-PA.

Sheng, K., Okuno, R., Imran, M., Nakutnyy, P., Nakagawa, K., 2021a. An Experimental Study of Steam-Solvent Coinjection for Bitumen Recovery Using a Large-Scale Physical Model. Presented in IOR 2021. European Association of Geoscientists & Engineers.

Sheng, K., Okuno, R., Al-Gawfi, A., Nakutnyy, P., Nakagawa, K., 2021b. An experimental study of steam-solvent coinjection for bitumen recovery using a large-scale physical model. SPE J. https://doi.org/10.2118/205158-PA.

Venkatramani, A., Okuno, R., 2017. Compositional mechanisms in SAGD and ES-SAGD with consideration of water solubility in oil. SPE Reservoir Eval. Eng. 20 (3), 681–697. https://doi.org/10.2118/180737-PA.

Venkatramani, A., Okuno, R., 2018a. Mechanistic simulation study of expanding-solvent steam-assisted gravity drainage under reservoir heterogeneity. J. Petrol. Sci. Eng. 169, 146–156. https://doi.org/10.1016/j.petrol.2018.04.074.

Venkatramani, A., Okuno, R., 2018b. Steam-oil ratio in steam-solvent coinjection simulation for homogeneous and heterogeneous bitumen reservoirs. J. Energy Resour. Technol. 140 https://doi.org/10.1115/1.4040529, 112903-1 – 112903-17.

Zirahi, A., Yamchi, H.S., Haddadnia, A., Zirrahi, M., Hassanzadeh, H., Abedi, J., 2020. 2-D physical model experimental study of ethyl acetate and steam Co-injection for in-situ bitumen recovery. Fuel 265. https://doi.org/10.1016/j.fuel.2019.116943, 116943.